



Technical Note

Global fiber reconstruction becomes practical

Marco Reisert^{a,*}, Irina Mader^b, Constantin Anastasopoulos^b, Matthias Weigel^a,
Susanne Schnell^a, Valerij Kiselev^a

^a Dept. of Radiology, Medical Physics, University Hospital Freiburg, Germany

^b Section of Neuroradiology, Neurocentre of University Hospital Freiburg, Germany

ARTICLE INFO

Article history:

Received 26 May 2010

Revised 16 August 2010

Accepted 9 September 2010

Available online 18 September 2010

Keywords:

Tractography

Global fiber tracking

Diffusion-weighted imaging

Q-Ball imaging

ABSTRACT

Global fiber reconstruction aims at providing a consistent view of the fiber architecture in the whole volume of cerebral white matter on the basis of diffusion-sensitized magnetic resonance imaging. A new realization of this principle is presented. The method utilizes data acquired with high angular resolution diffusion imaging (HARDI), a measurement method that fulfills clinical requirements. For the first time among global reconstruction methods, the computation time is acceptable for a broad class of practical applications. The method does not involve any boundary conditions that prescribe the location of the ends of reconstructed fibers. This helps to minimize necessary user interaction and operator dependence. Results obtained in a physical phantom demonstrate a high reconstruction quality. In vivo results have been obtained in several volunteers. The algorithm found a number of prominent fascicles including those in the limbic system, which had been problematic for a previously published version of global tracking.

© 2010 Elsevier Inc. All rights reserved.

Introduction

Fiber tracking is a method for the reconstruction of neuronal pathways based on measurements of the anisotropic diffusion of water molecules in the fibrous structure of white matter (Moseley et al., 1990; Conturo et al., 1999; Mori et al., 1999; Basser et al., 2000). Such information is available by diffusion-weighted magnetic resonance imaging (MRI). Fiber tracking promises to have a high impact in fundamental neuroscience and its clinical applications.

The approaches can be divided into two groups: local and global methods. Local methods construct fibers independently path-by-path; the fibers do not influence each other. The reconstruction of long neuronal pathways is performed in small successive steps, either deterministically (Mori et al., 1999; Basser et al., 2000) or probabilistically (Hagmann et al., 2003; Parker et al., 2003) by following the local, voxelwise defined distribution of fiber directions. This distribution is described by the **orientation distribution function (ODF)**, the determination of which is the first step in the majority of suggested tracking methods. The advantage of local methods is that they are rather fast, but they also have several problems. The most apparent is probably that minor imperfections in the determination of local steps can accumulate and significantly affect the final result. Such an error can arise from the uncertainty in the determination of the ODF from the diffusion data, which is a very difficult, ill-posed problem.

On the other hand, global methods try to reconstruct the fibers simultaneously by finding the configuration that describes best the measured data. This necessarily involves the solution of the **forward problem of predicting the measured signal given a fiber configuration**. The optimization of the fiber configurations with respect to the data resolves implicitly the inverse problem of finding the microscopic structure using the diffusion-weighted MRI. In general, this problem has many solutions. Selecting a suitable one requires prior knowledge about the expected properties of neuronal fibers such as the absence of branching, termination at definite anatomical structures etc. Global tracking thus avoids an explicit solution of the inverse problem and promises a better stability with respect to noise and imaging artifacts. The **main problem** of global methods is a very long **computation time**, often unacceptable in the clinical setting. A further problem is the arbitrariness in defining prior knowledge. Specification of prior knowledge that is too detailed might lead to inconsistencies with the actual data, or user-intervention that is too subject-specific.

Here, we suggest a new realization of global tractography with the focus on model simplicity and computational performance. The basic idea shares some properties with other recent global tracking algorithms (Mangin, 2002; Kreher et al., 2008; Fillard et al., 2009): The reconstructed fibers are built with small line segments that introduce the diffusion anisotropy. These elemental segments bind together during the optimization. Their orientation and number are adjusted simultaneously to match the data. This behavior is governed by an interaction between line elements and by an increasing match to the measured data. We found a **new form of these rules** which has resulted in an increase in computational performance by two orders of magnitude, thus enabling practical applications for global

* Corresponding author.

E-mail address: marco.reisert@uniklinik-freiburg.de (M. Reisert).

tracking. An important difference to previous studies (Kreher et al., 2008; Fillard et al., 2009) is the **absence of any boundary conditions**, which minimizes the dependence on the operator and keeps the necessary user interaction low. Our method is currently designed to process data obtained by high angular resolution diffusion imaging (HARDI), which is most suitable for applications in the clinical environment.

Materials and methods

We denote the set of all line elements, the fiber model, by \mathcal{M} . The measurement data is denoted by $D(\mathbf{x}, \mathbf{n}) = S(\mathbf{x}, \mathbf{n}) / S_0(\mathbf{x})$, where $S(\mathbf{x}, \mathbf{n})$ is the diffusion-weighted, HARDI signal at position \mathbf{x} with gradient direction \mathbf{n} at a fixed b-value. By $S_0(\mathbf{x})$ is denoted the measurement without diffusion weighting, typically the average of several measurements with b-value equal to zero. The aim of the optimization is to **maximize** the a-posteriori probability $P(\mathcal{M}|D)$ with respect to \mathcal{M} , that is to find the most likely model given the observed data. We follow Bayes' theorem and assume the usual exponential form for the prior $P(\mathcal{M})$ and data-likelihood $P(D|\mathcal{M})$:

$$P(\mathcal{M}) = e^{-E_{\text{int}}(\mathcal{M})/T}, P(D|\mathcal{M}) = e^{-E_{\text{ext}}(\mathcal{M}, D)/T}.$$

Here E_{int} controls the behavior of line segments, in particular driving them to build long fibers, E_{ext} expresses the similarity of the model with respect to the data. These quantities are termed “energy” in spirit of statistical physics. In the same way, the parameter T is termed the temperature. Maximizing the probability is equivalent to finding the minimum of the total energy $E(\mathcal{M}) = E_{\text{int}}(\mathcal{M}) + E_{\text{ext}}(\mathcal{M}, D)$. To find the minimum of $E(\mathcal{M})$ we use a so-called **Metropolis Hastings sampler** (Neal, 1993; van Lieshout, 2000).

The model

We consider now the basic building blocks of the fiber model \mathcal{M} . The model consists of small line (fiber) segments that can form chains to represent the individual fibers. Reconstructions which we are aiming for will sometimes contain **several hundred of these segments per voxel**. Each segment is described by a continuous spatial position $\mathbf{x} \in \mathbb{R}^3$ and an orientation $\mathbf{n} \in S_2$. Formally, we refer to a fiber segment by the tuple $X_i = (\mathbf{x}_i, \mathbf{n}_i)$. Picture the fiber segment as a small thin tube of length 2ℓ , i.e. the endpoints of the tube are at position $\mathbf{x} + \ell\mathbf{n}$ and $\mathbf{x} - \ell\mathbf{n}$, respectively (Fig. 1). These endpoints can make connection with endpoints from other segments, they generate the chains that form the fibers of the model. We refer to the two endpoints of a segment X by X^+ and X^- , respectively. Thus, a connection E between two endpoints is described by a tuple $E = (X_1^{\alpha_1}, X_2^{\alpha_2})$. In these notations, $\alpha = \{-, +\}$ defines the direction along the segment, in mathematical expressions it should be treated as a factor $\alpha = \pm 1$. The **fiber model** \mathcal{M} is the set of all segments $\mathcal{X} = \{X_i\}$ together with the set of all connections denoted by $\mathcal{E} = \{E_j\}$. From the arrangement of all

segments a predicted MR-signal is computed. Each segment contributes additively to this signal with a prototype-signal of

$$\rho_{X_i}(\mathbf{x}, \mathbf{n}) = e^{-c(\mathbf{n}^T \mathbf{n}_i)^2} e^{-|\mathbf{x} - \mathbf{x}_i|^2 / \sigma^2},$$

where \mathbf{n}_i and \mathbf{x}_i are the orientation and position of the segment. This means that the segment forms a usual stick model in orientation space and an isotropic Gaussian in the spatial domain. The parameters $\sigma > 0$ and $c > 0$ describe the ‘shape’ of the prototype-signal.

Internal energy

The internal energy controls the connection behavior between the segments. Each segment can make, with both of its endpoints, connections to other segments. **If** two segments are **connected**, they feel a certain **attraction force** such that they **stay nearby** and keep their orientations similar. They do not attract other segments. Thus, the internal energy is a sum over all connections:

$$E_{\text{int}}(\mathcal{M}) = \sum_{(X_1^{\alpha_1}, X_2^{\alpha_2}) \in \mathcal{E}} U_{\text{con}}(X_1^{\alpha_1}, X_2^{\alpha_2})$$

where $U_{\text{con}}(X_1^{\alpha_1}, X_2^{\alpha_2})$ refers to the interaction potential. To define the interaction potential between two connected segments, we use the abbreviation $\bar{\mathbf{x}} = (\mathbf{x}_1 + \mathbf{x}_2) / 2$ for the midpoint of the line connecting the two segments. We found quite a simple interaction potential which drives the segments to stay together and keep their orientation similar:

$$U_{\text{con}}(X_1^{\alpha_1}, X_2^{\alpha_2}) = \frac{1}{\ell^2} \left(\|\mathbf{x}_1 + \alpha_1 \ell \mathbf{n}_1 - \bar{\mathbf{x}}\|^2 + \|\mathbf{x}_2 + \alpha_2 \ell \mathbf{n}_2 - \bar{\mathbf{x}}\|^2 \right) - L.$$

Basically, the potential is composed of the squared distances from the endpoints of the segments to the midpoint of the line connecting both. For an illustration see Fig. 1. The two parameters that occur are the length $\ell > 0$ (actually half the length) of the fiber segment and a bias L . The bias L is a kind of connection likelihood. Large $L > 0$ imply a high likelihood that two segments link together.

External energy

The external energy is the squared **difference between** the actual **signal S** and the **predicted signal**

$$\rho_{\mathcal{M}}(\mathbf{x}, \mathbf{n}) = w \sum_{X_i} \rho_{X_i}(\mathbf{x}, \mathbf{n}),$$

where $w > 0$ is a weight with which each segment contributes. Note that the contribution of each segment is the same. Prior to comparison of both signals, the local mean is subtracted, i.e. $\rho' = \rho - \int \rho d^2 \mathbf{n} / (4\pi)$ and the same for the data D . Thus, the external energy is the $L_2(\mathbb{R}^3 \times S_2)$ -norm of the meaningless signal difference:

$$E_{\text{ext}}(\mathcal{M}, D) = \|\rho'_{\mathcal{M}} - D'\|_{L_2(\mathbb{R}^3 \times S_2)}^2.$$

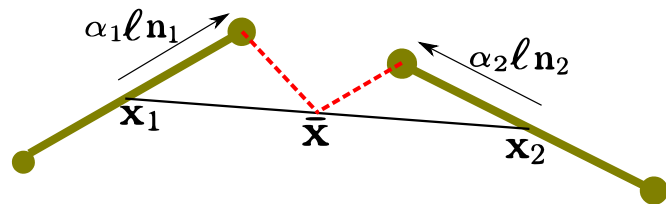


Fig. 1. Two line segments and the elements for constructing their internal energy. The segments are given by their midpoints $\mathbf{x}_1, \mathbf{x}_2$ and their orientations $\mathbf{n}_1, \mathbf{n}_2$. The red dotted lines indicate the distances whose sum of square defines the internal energy.

This implies that the isotropic component does not affect the energy. A similar approach was used by Kreher et al. (2008). We need this freedom because the value of the local mean of the measurement is not an indicator for the true number of segments per voxel. The energy E_{ext} forces the model to be close to the measurement in anisotropic areas where the data interpretation is unambiguous, while the number of segments in isotropic areas is ‘free’ as long as they are isotropically distributed. Together with the internal regularization energy E_{int} , this approach infers information in ambiguous isotropic areas from the neighboring anisotropic areas.

Optimization

To minimize the above formulated objective, we rely on a kind of **simulated annealing approach**. More precisely, we use a Metropolis Hastings sampler (Neal, 1993) to draw samples from the posterior distribution

$$P(\mathcal{M}|D) \propto P(D|\mathcal{M})P(\mathcal{M})e^{-E(\mathcal{M})/T}.$$

By lowering the temperature T , it becomes more and more likely to sample from maxima of $P(\mathcal{M}|D)$ which correspond to minima of $E(\mathcal{M})$. The idea of the Metropolis Hastings sampler is to choose certain state transitions randomly. These transitions are chosen according to certain proposal distributions. The approach is as follows: choose a modification of the current state \mathcal{M} according to a proposal distribution p^{prop} , we call this modification \mathcal{M}' . Then, accept this modification if the so-called Green's ratio R is above 1, where R is given by

$$R = \frac{P(\mathcal{M}'|D)p^{\text{prop}}(\mathcal{M}|\mathcal{M}')}{P(\mathcal{M}|D)p^{\text{prop}}(\mathcal{M}'|\mathcal{M})}. \quad (1)$$

If R is below 1, the modification is accepted with probability R . Note also that $p^{\text{prop}}(\mathcal{M}|\mathcal{M}')$ appears in the numerator of R , i.e. it is imperative that $p^{\text{prop}}(\mathcal{M}|\mathcal{M}') \neq 0$ to get a non-vanishing probability that the transition actually occurs. This demand is the so-called reversibility property. It is important to keep this restriction in mind while designing the proposal distribution. After a certain number of iterations (the 'burn-in' phase) the resulting chain of states follows the desired distribution. Then, the temperature is slowly decreased. To stop the iteration, we look currently at two quantities: the ratio of the connections versus the number of segments, and the distribution of fiber length. Once both have converged to a kind of stable state the iteration is stopped. For further details see Reisert et al. (2009); Neal (1993); van Lieshout (2000).

In our approach, the proposal splits into three different types, where each of the proposal is selected with a certain probability: segment creation/deletion ($p_{\text{birth}}, p_{\text{death}}$), segment moves ($p_{\text{shift}}, p_{\text{opt}}$) and segment connections (p_{fiber}). Pseudocode of the algorithm is given below. Segment creation/deletion and moves follow standard techniques (Reisert et al., 2009; Kreher et al., 2008), only the proposal of how to create connections is different, so we give some details in the next section.

Algorithm 1 Optimization

Input: Start with empty reconstruction \mathcal{M}
Output: fiber reconstruction \mathcal{M}
 1: **for** $j = 1$: #iterations **do**
 2: Select one of the proposals according to the probabilities $p_{\text{birth}}, p_{\text{death}}, p_{\text{shift}}, p_{\text{opt}}, p_{\text{fiber}}$
 3: According to proposal type, generate new state \mathcal{M}'
 4: Compute Green's ratio according to Eq. (1)
 5: **if** $R > \text{random number} \in [0, 1]$ **then**
 6: $\mathcal{M} := \mathcal{M}'$
 7: **end if**
 8: Reduce the temperature
 9: **end for**

Creating connections

The way of generating connections $E \in \mathcal{E}$ between segments is partially based on a common local tracking algorithm. The proposal does not propose just one connection E but a whole set of connections forming the part of a putative fiber. By a fiber part, we think of a sequence of connections $f = (E_1, E_2, \dots)$ which connect fiber segments X_k consecutively. In these terms the actual proposal is as follows: select uniformly an existing $(\mathbf{x}, \mathbf{n}) = X_0 \in \mathcal{X}$ and a direction $\alpha = \{-, +\}$. Now delete the connections of the fiber starting at X_0^α up to a certain

length, which is determined in a probabilistic manner. Now a new fiber f_{new} starting at X_0 is proposed. The proposed fiber is a result of a probabilistic hopping procedure on the already existing segments, similar to known probabilistic tracking algorithms. Finally, it is decided by Green's ratio whether the old fiber is replaced by the new one or the old state is kept.

Parameters

The introduced method depends on several parameters. The influence of these parameters will now be discussed. First, we look at the 'geometrical' model parameters: the prototype-signal of an individual segment depends on the width σ and the orientation sharpness c . They both **control the expected number of fibers** of the reconstruction. A small choice for σ results in a high number of reconstructed fibers. During the experiments we found that a range between 0.5 mm and 1 mm in human brains produces a reasonable number of segments with respect to computation time and complexity of the reconstruction. In voxel units, this is about half to a fifth of a voxel side length (for typical spatial resolutions), corresponding to a expected number of **segments per voxel** of about **2³ to 5³**. For a higher number of segments, the optimization becomes currently intractable.

To find values for c , consider a measurement in the corpus callosum as the most anisotropic part of the brain. In this region, one usually observes signals like $S/S_0 \approx e^{-bD(n^T n_i)^2} \approx e^{-(n^T n_i)^2}$ with a bD of approximately 1. There are two possible approaches to modeling such a signal. In the macroscopic view, one can try to model the signal in a voxel all at once by one or a few segments. On this way, the signal conurbation should depend on the experimental b-factor and it would be difficult to comply with the natural local variations of the diffusion coefficient. In this work, we chose the microscopic view, in which each segment contributes a much 'sharper' signal than in the corpus callosum. The observed signal is then modeled by an ensemble of non-collinear segments, in which each segment alone is not able to explain the signal. For example, in the corpus callosum, the group of segments inside a voxel fluctuate around one strong mean direction. The fluctuation leads to a broadening of the predicted signal. The same argument holds for a variation in the diffusion coefficient. This approach makes the model parameters more or less independent of the b-value of the measurement, because if the width of the measured orientation distribution, for instance, gets smaller (high b-values), the reconstructed fibers just get more aligned to the data. The microscopic view requires the prototype-signal from a single segment to be more anisotropic than the signal in corpus callosum, which implies a large c . We found values of $c = 5^2$ to work well. This is about a fifth of the orientation distribution width of typical values for the brain.

The **segment length ℓ** controls the **expected curvature** of the fibers. Large ℓ imply low curvature and vice versa. It is obvious that ℓ and σ have to be interrelated. We found that $2\sigma < \ell$ has to hold. Values of σ that are too large obviously prevent the segments from being connected. Note that curvature and the discretization of the fiber are inherently connected, which is reasonable because fibers with low curvature only need a rather rough discretization while fibers with high curvature need a fine discretization.

Besides these geometry related parameters, there are two other model parameters, these are the connection bias L and the value of the weight w . The connection bias L is just the likelihood that two segments become connected. Large values imply very 'curly' reconstructions with lots of false positive connections, while small L result in rather short fibers. Besides σ and ℓ , the **weight w** is a third parameter, which controls the **expected number of segments**. For low values of w , the reconstruction needs more segments to 'explain' the same signal portion than for high values. The interplay of w , σ and c is probably the most crucial part for obtaining good results. To get a rough estimate for w , in a more or less automatic way, one can consider the standard deviation s of the meaningless signal. We found

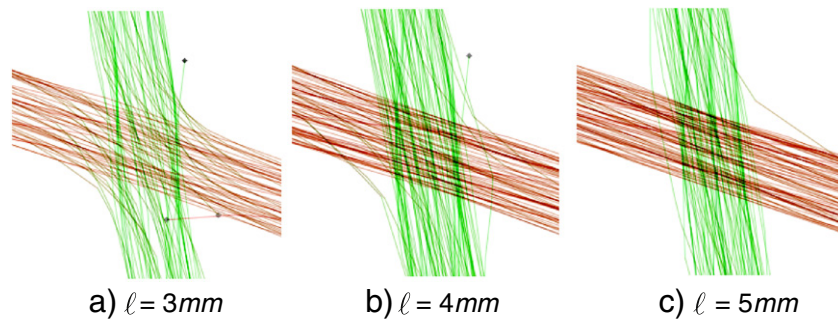


Fig. 2. Reconstructions of a simulated crossing for different segment lengths. For long segments (low curvature implied) the crossing is easily resolved while for short segments the crossing is increasingly interpreted as a kissing configuration. Fiber terminals are indicated by black dots.

that a choice of $0.2 \cdot s < w = 0.5 \cdot s$ is reasonable. For higher weights w , the segments get very sparsely distributed. Weights below $0.2 \cdot s$ imply a huge number of segments which are not computationally tractable anymore.

Another group of parameters are the iteration parameters and the parameters that appear inside the proposal distributions. They include the number of iterations, the temperature schedule, and the individual proposal probabilities p_{birth} , p_{death} , p_{shift} and p_{fiber} . For the proposal we used the following probabilities: $p_{\text{birth}} = 0.25$, $p_{\text{death}} = 0.05$, $p_{\text{shift}} = 0.15$, $p_{\text{opt}} = 0.1$, $p_{\text{fiber}} = 0.45$. Note that the result of the reconstruction does not depend on these probabilities, they just influence the number of iterations needed to get a stable result. The number of iterations depends mainly on the reconstruction complexity. For instance, if we expect a very dense reconstruction (small σ), we have to choose a high number of iterations (for a whole-brain reconstruction about $i_{\text{max}} = 10^9$). For sparse reconstructions 10^8 iterations are enough. The temperature schedule is typically exponential $T(i) = T_0 e^{-\alpha i}$ where the starting temperature is usually $T_0 = 1$. The stop temperature $T(i_{\text{max}})$ should be quite low. We found that values of $T(i_{\text{max}}) = 10^{-3}$ are a reasonable choice. For temperatures below this point the state changes become very unlikely, that is, the fiber model is ‘frozen’ at this point. For higher temperatures the fibers are still curly and not smooth.

Phantom and in vivo data

The phantom data (Poupon et al., 2008) was acquired on the 3T Tim Trio MRI systems. A single-shot diffusion-weighted twice-refocused spin echo echoplanar pulse sequence was used to perform the acquisitions. For our experiment, we used the 3 mm resolution dataset with a field of view $FOV = 19.2\text{cm}$ and a $b = 2000\text{s/mm}^2$ corresponding to the echo time $TE = 102\text{ms}$. The diffusion sensitization

was applied along a set of 64 orientations, uniformly distributed over the sphere. For more details on the phantom data, see Poupon et al. (2008). The FA-values of the phantom are quite low, which makes on the one hand the tracking problem challenging, but on the other hand, this challenge does not reflect all problems of the in vivo reconstruction. As default we use the following geometrical parameters in our experiments: $\sigma = 1.5\text{mm}$ and $\ell = 4\text{mm}$. That is, a fiber segment is a little shorter than three voxel units. The orientation sharpness was chosen to be $c = 2 \cdot 25 = 50$. The weight was chosen, as suggested above, according to the standard deviation of the meaningless signal, namely $w = 0.25 \cdot s$. The connection bias was chosen to be $L = 1$, that is the internal energy of two connected collinear segments with the distance between their endpoints $\sqrt{2}\ell$ is zero. The reconstruction domain was determined by a thresholded b_0 image, where we additionally masked out manually the outer rim of the phantom. The rim showed high FA-values and would disturb the reconstruction.

The in vivo diffusion measurements were acquired on a Siemens 3T TIM Trio using an SE EPI sequence, with a TE of 95 ms and a TR of 8.5 s. The whole brain was covered with contiguous 2 mm slices with an in-plane resolution of $2 \times 2\text{mm}^2$. The diffusion encoding was performed in 61 directions with an effective b-value of 1000s/mm^2 . Additionally, a T_1 data set was acquired which was segmented into white matter (WM), gray matter (GM), and CSF using SPM5. The parameters of the method are similar to the phantom: typical values for the geometric parameters are $\sigma = 1\text{mm}$ and $\ell = 4\text{mm}$. The orientation sharpness was chosen to be $c = 25$ and the w again between $w = 0.2\text{s}$ for a dense reconstruction and $w = 0.5\text{s}$ for sparse reconstruction. The connection bias was also chosen to be $L = 1$. A WM mask was computed from a coregistered and segmented T_1 image. Actually, our method does not require a clean WM mask, a rough estimate of a brain mask is also enough to get reasonable results.

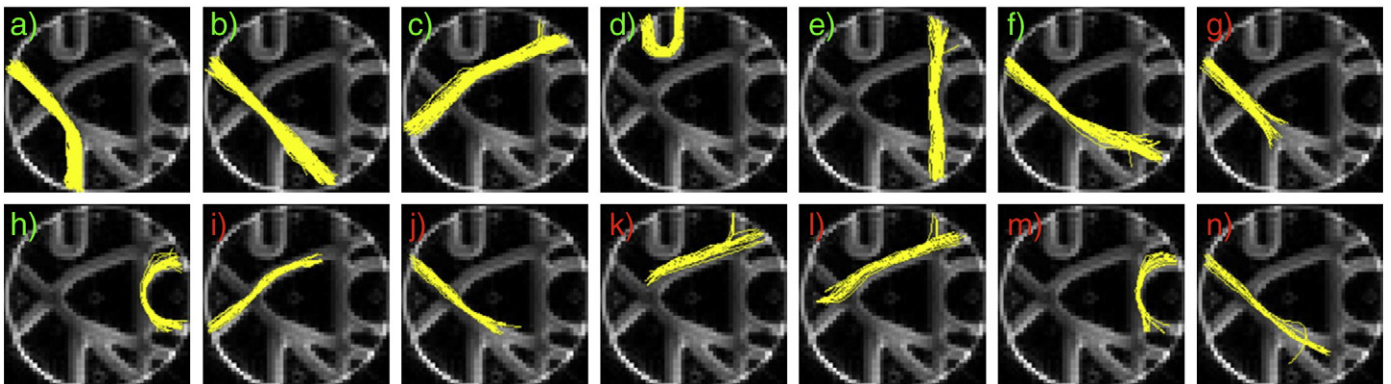


Fig. 3. The reconstruction of the phantom was clustered into coherent fiber bundles. The 14 most prominent bundles are shown. It is clear that the existing bundles are resolved but some short fiber stubs are also present.

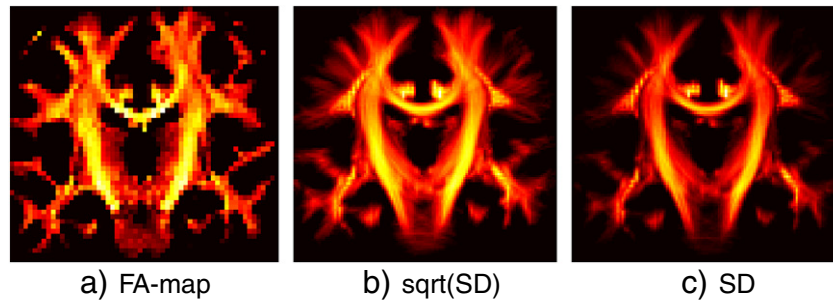


Fig. 4. A usual FA-map in original resolution (a) compared with the segment density (b) and (c) with double resolution. The square root of the segment density (b) is taken to better display the domain of low intensities. In most regions the segment density is similar to the FA-map. Differences appear in crossing regions where FA is low.

Results

Before looking at the physical phantom, we illustrate how our method resolves fiber crossings using a simulated phantom. The fiber data was generated on a voxel grid of 3 mm resolution with a bundle width of 10 mm. The orientation ‘width’ was chosen with respect to the product $bD = 1$. In Fig. 2, we show reconstructions for a varying segment length ℓ . For long segments (implying low curvature), the crossing is nicely resolved, while for small segments the crossing is getting increasingly strongly like a kissing configuration. Note that a few ‘broken’ fibers with endpoints somewhere around the crossing also start to appear, in particular, for a low ℓ -parameter.

Phantom

We did a reconstruction of the physical phantom according to the parameters described above. For visualization the reconstructed fibers were grouped into meaningful subbundles by unsupervised clustering. A simple hierarchical clustering was used, the fiber distance measure of which is computed by point-by-point L_2 -distances between normalized arc length parametrized fibers. In Fig. 3, we show the 14 most prominent clusters obtained from this analysis. They are ranked from a) to n) by the within-cluster coherence measure. One can see that all of the correct fiber bundles are present, namely a), b), c), d), e), f), and h). All the crossings are nicely resolved. What is particularly remarkable is the sharp U-turn (Fig. 3d)) bundle which is also clearly represented, and shows only a few overshooting fibers. But there are also, as one might expect, some bundles that represent short sections of longer bundles.

At the MICCAI’2009 this phantom was used in the DMFC-fiberCup (see www.inao.fr/spip.php?article159) for the comparison of different tracking algorithms. The proposed algorithm achieved the best results within a group of 10 participants. Besides our approach, the methods of Malcolm et al. (2009) and Jeurissen et al. (2009) gave competitive results. Both approaches are based on a deterministic tracking algorithm. Where the approach of Malcolm et al. (2009) is based on Kalman-filtering to simultaneously fit a local model to the signal and propagate in the most consistent direction, in Jeurissen et al. (2009), the fiber orientation distributions are estimated by constrained spherical deconvolution (Tournier et al., 2007) together with an adaptive anisotropic Gaussian filter. In comparison to our approach, the pathways of the reconstructed fibers were qualitatively similar, but our approach gave much more accurate results in terms of position, tangent directions and curvature of the reconstructed fibers.

In vivo data

We start with a sparse reconstruction of the whole brain with a rather short reconstruction time of several minutes on a standard PC. The parameters were chosen as described in Phantom and in vivo data section where the weight was chosen to be $w = 0.5 \cdot s$. We found that

all parameters are quite stable over different subjects. Typical reconstructions contain approximately 5000 fibers longer than 5 segments (i.e. longer than 20 mm). For 95% of these fibers, the endpoints are both located in a gray matter mask determined from a T_1 -weighted image. To get a more dense reconstruction, we reduced the segment weight to $w = 0.2 \cdot s$, which results in a reconstruction time of a few hours on a standard PC and gives fiber numbers of approximately 10^5 (Fig. 4).

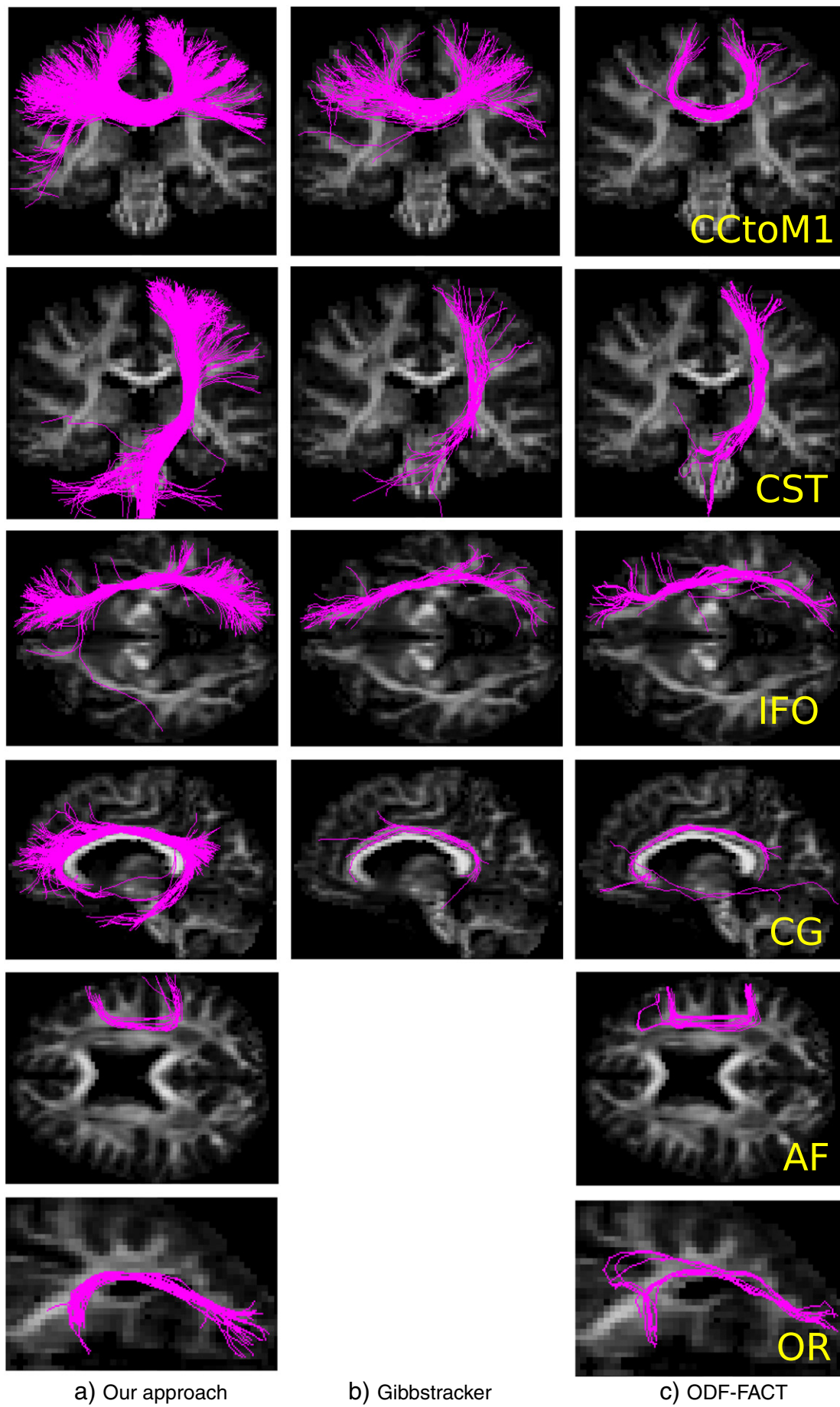
To analyze such a huge reconstruction, we used several ROIs to extract well known fiber bundles. In Table 1, the positions of the ROIs are summarized. In particular, we considered the part of the callosal fibers coming from the left motor cortex (CctoM1), corticospinal tracts to the left motor cortex (CST), the inferior fronto-occipital fasciculus (IFO) the cingulum (CG), the arcuate fasciculus (AF), and the optic radiation fibers (OR). Based on the whole-brain reconstruction with segment length $\ell = 4$ mm, we selected the above mentioned fiber bundles by demanding that each fiber within the bundle visit both ROIs. In Fig. 5, the results of our approach are compared with the Gibbstracker and a deterministic tracker (Mori et al., 1999) based on ODFs extracted from the HARDI data following Aganj et al. (2009). For CST and CF(M1), our approach and the Gibbstracker create similar results, while for the deterministic approach, all the lateral projections are missing. Another difference appears for the CctoM1, where, in contrast to our method, the Gibbstracker has relatively less fibers going to the apical cortex. For the IFO, the deterministic tracker and the Gibbs tracker perform similarly, while our approach shows more widespread projections. Big differences appear for the CG. Our approach shows many more fibers in the cingulum, while it seems to be very difficult for the Gibbstracker and the deterministic tracker to find any. For the AF and OR the Gibbstracker was not able to find any in the whole-brain reconstruction, while our approach and the deterministic tracker were able to detect them.

In Fig. 6, we take a closer look at the transcallosal fibers. The cortical projections of the transcallosal fibers for different viewpoints

Table 1

The ROIs used for selecting the considered bundles. The ROIs were derived from the WFU PickAtlas (Maldjian et al., 2003), from the literature, where the coordinates were given in MNI space (Saur et al., 2008) or manually according to (Kreher et al., 2008).

Bundle	ROIs	Source
CctoM1	Precentral gyrus	WFU
	Corpus callosum	Manual
CST	Precentral gyrus	WFU
	Posterior limb of the internal capsule	Manual
IFO	Anterior fronto-occipital fascicle	Manual
	Posterior fronto-occipital fascicle	Manual
CG	Anterior cingulate cortex	Manual
	Posterior cingulate cortex	Manual
AF	Posterior superior temporal gyrus (T1p)	Saur et al.
	Inferior frontal gyrus, pars opercularis (F3op)	Saur et al.
OR	Lateral geniculate nucleus	WFU
	Primary visual cortex	WFU



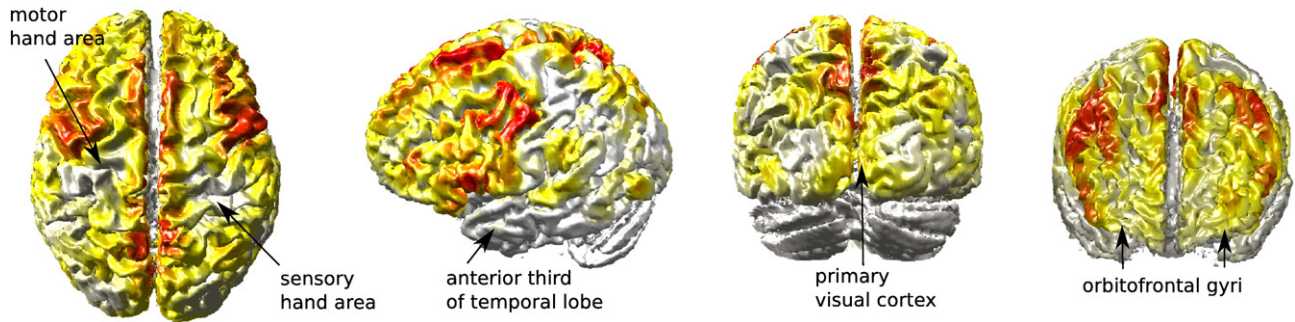


Fig. 6. Cortical projections of the transcallosal fibers from different viewpoints. All fibers passing the corpus callosum were selected and the density of endpoints on the cortex visualized. For certain areas, like the sensory and motor hand area, the anterior third of the temporal lobe, parts of the visual cortex and the orbitofrontal gyri, there is a scarcity of projections. Predominant projections are in the premotor and primary motor area of the head and trunk.

are shown. For certain areas, like the sensory and motor hand area, parts of the orbitofrontal gyri and the anterior third of the temporal lobe, there is a scarcity of projections. Predominant projections appear in the premotor and primary motor area of the head and trunk.

Finally, in Fig. 4, we show for a coronal section a map displaying the number of segments per voxel compared with a FA-map. The number of segments is closely related to FA. Remarkably, deviations appear in the crossing regions, where FA is relatively lower, and in peripheral regions where FA is relatively higher than the observed segment density.

Discussion

The method of fiber tracking presented in this study realizes global fiber reconstruction with little manual interaction and prior assumptions. To our knowledge, for the first time among global tracking methods, the computation time for a whole-brain reconstruction is acceptable for many types of clinical applications. The major challenge of global fiber reconstruction, as an inverse problem, is the restricted information provided by HARDI measurements. There are basically two ways to introduce prior knowledge, in terms of boundary conditions or as a regularization term. The present solution relies on regularization involving no boundary conditions for the termination of fibers.

We started our investigations with a simple consideration of a synthetic crossing region. Obviously, the results depend on the parameter ℓ , which is directly related to the expected curvature of the fibers. For large ℓ , it is easy for the algorithm to resolve the crossing, while for short ℓ , the configuration is increasingly interpreted as a kissing configuration. Similar to existing tracking algorithms, there is also this trade-off between a low curvature setting to resolve the crossings, and a high curvature setting to cope with sharp bends. On the other hand, introducing prior knowledge about the expected curvature of the fibers is necessary to resolve crossings, in particular in a low b-value regime. So, we have to emphasize that this parameter must be handled carefully. Fortunately, we were also able to show with the physical phantom that both the crossings and a sharp U-turn can be resolved with one fixed ℓ parameter. The results on the physical phantom are convincing, apart from the problem that some fibers end elsewhere in the reconstruction area (which models the white matter). But, as shown by the clustering of the reconstruction into subbundles, the correct bundles are very prominent and are detected first.

To solve the problem completely, one could set boundary conditions (BC) such that fibers are only allowed to end at specific locations at the rim of the phantom. Such a solution was used in two recent global reconstruction approaches (Fillard et al., 2009; Kreher et al., 2008). This is

an advantage for the optimization algorithm because it can start 'tracking' at certain predefined 'seeds' in the cortex. The main problem with this way is that it is quite difficult (maybe at the moment impossible) to determine the 'true' boundary conditions or seeds in the brain including also the deep gray matter structures. On the other hand, we have observed that even without any boundary conditions up to 95% of the fibers connect voxels in gray matter with other voxels in gray matter.

Our results suggest that the global cartography of the brain can be biased by the BC. There are big differences for the AF, CG and OR, which might be explained by the use of the boundary conditions inside the Gibbstracker. The Gibbstracker favors reconstructions with fiber endings evenly distributed over the cortex. This inhibits higher concentrations of fiber endings at certain locations. The Gibbstracker does not appear to perform well when it is required to find bundles where the determination of the WM/GM transition mask is problematic due to the complex folded anatomy of the cortex. This, in particular, happens for the cingulum (CG) or the optic radiation fibers (OR), where the determination of the lateral geniculate body is difficult. Both are found by our approach in a definite manner, while the Gibbstracker has problems with the CG and is unable to detect the OR in a whole-brain reconstruction.

Callosal projections are a problem for each tracking algorithm. 80% of the callosal fibers are described to have an axial or para-axial body representation, and 28% alone represent the head region (Guillemot et al., 1987). It seems to be widely accepted that inter-hemispheric connections of motor areas are necessary for the execution and coordination of complex movements (Boussaoud et al., 2005). But only weak callosal connections of the M1 hand area are found (Guillemot et al., 1987). Thus, all proposed tracking methods show an imperfect image of the callosal fiber connections: ODF-FACT shows only callosal projections of the extremities being wrong in the above described context. The Gibbstracker predominantly connects the hand area, a result which is also not truly related to the anatomical knowledge. Our approach shows the most wide spread connections, also finding head, trunk and foot regions. Thus, our approach shows the highest potential, but has to be optimized for particular anatomical purposes.

In conclusion, we do not claim that a global BC-free method is always the better choice. But it seems that as long as we do not use a modality that reflects the number of fiber endings in the cortex, it is quite dangerous to assume 'some' boundary condition. Further, it is much easier from a user's point of view to take a white matter mask and the DTI data and start tracking, instead of a laborious determination of boundary conditions that, in the end, may not even be stable between subjects. Also, for group studies, a less operator dependent approach is much better suited. The problem of our BC-free method is that we have a number of fibers that end

Fig. 5. The six considered bundles tracked with our approach (a), the Gibbstracker (b) and a HARDI-based deterministic tracker (c). The fibers are shown in magenta, the underlying image is an FA-map. From top to bottom: A part of the callosal fibers coming from the left motor cortex (CCToM1), the cortical spinal tracts projecting to the motor cortex (CST), the inferior fronto-occipital fasciculus (IFO), the cingulum (CG), part of the arcuate fasciculus (AF) and the optic radiation fibers (OR).

somewhere within white matter. Depending on the parameters up to 5 to 10% of fibers were measured, in which both endpoints did not end in the gray matter area. Filter and clustering techniques may be applied at this point. On the other hand, the present method works reasonably well even without such ‘clean-up’ post-processing, being able to find several prominent structures (CST, CCtoM1, CG, IFO, AF, OR) and resulting in detected fibers that are sufficiently long to connect the corresponding cortical areas.

The proposed technique was implemented in C++ and is publically available within the DTI and fibertools package (Kreher et al., 2006) together with a simple graphical user interface.

Acknowledgments

The work of M. Reisert was supported by the European Commission, contract 027294 (I-KNOW) and by the Deutsche Forschungsgemeinschaft (DFG), grant KI 1089/3-1. Further acknowledgments go to Björn Kreher for providing the ROIs and Kuan J. Lee for proofreading.

References

- Aganj, I., Lenglet, C., Sapiro, G., 2009. Odf reconstruction in q-ball imaging with solid angle consideration. *Proceedings of IEEE Int. Symposium on Biomedical Imaging*. Bassar, P.J., Pajevic, S., Pierpaoli, C., Duda, J., Aldroubi, A., 2000. In vivo fiber tractography using DT-MRI data. *Magn. Reson. Med.* 44 (4), 625–632 (20481737 0740-3194 Journal Article).
- Boussaoud, D., Tanne-Gariepy, J., Wannier, T., Rouiller, E., 2005. Callosal connections of dorsal versus ventral premotor areas in the macaque monkey: a multiple retrograde tracing study. *BMC Neurosci.* 6 (1), 67 (URL <http://www.biomedcentral.com/1471-2202/6/67>).
- Conturo, T.E., Lori, N.F., Cull, T.S., Akbudak, E., Snyder, A.Z., Shimony, J.S., McKinstry, R.C., Burton, H., Raichle, M.E., 1999. Tracking neuronal fiber pathways in the living human brain. *Proc. Natl. Acad. Sci. USA* 96 (18), 10422–10427 (0027-8424 (Print) Journal Article Research Support, Non-U.S. Gov't Research Support, U.S. Gov't, P.H.S.).
- Fillard, P., Poupon, C., Mangin, J.-F., 2009. A novel global tractography algorithm based on an adaptive spin glass model. *Proceedings of MICCAI*. Vol. 1, pp. 927–934.
- Guillemot, J.-P., Richer, L., Prevost, L., Ptito, M., Lepore, F., 1987. Receptive field properties of somatosensory callosal fibres in the monkey. *Brain Res.* 402 (2), 293–302 (URL <http://www.sciencedirect.com/science/article/B65YR-4836-0TT-1TV/2/e89afb6f1ae5011da4e0de36993137a2>).
- Hagmann, P., Thiran, J.P., Jonasson, L., Vanderghenst, P., Clarke, S., Maeder, P., Meuli, R., 2003. Dti mapping of human brain connectivity: statistical fibre tracking and virtual dissection. *Neuroimage* 19 (3), 545–554 (english 1053-8119).
- Jeurissen, B., Leemans, A., Tournier, J.-D., Sijbers, J., 2009. Fiber tracking on the fiber cup phantom using constrained spherical deconvolution. *Proceedings of the DMFC Workshop*. MICCAI.
- Kreher, B.W., Hennig, J., Il'yasov, K.A., 2006. DTI-Fibertools: a complete toolbox for DTI calculation, fiber tracking, and combined evaluation. *Proceedings of the 12th Annual Meeting ISMRM Seattle*. ISMRM, Berkeley, CA, p. 2758.
- Kreher, B.W., Mader, I., Kiselev, V.G., 2008. Gibbs tracking: a novel approach for the reconstruction of neuronal pathways. *Magn. Reson. Med.* 60 (4), 953–963.
- Malcolm, J.G., Shenton, M.E., Rath, Y., 2009. Filtered tractography: validation on a physical phantom. *Proceedings of the DMFC Workshop*. MICCAI.
- Maldjian, J.A., Laurienti, P.J., Kraft, R.A., Burdette, J.H., 2003. An automated method for neuroanatomic and cytoarchitectonic atlas-based interrogation of fMRI data sets. *Neuroimage* 19 (3), 1233–1239 (1053-8119 (Print) Journal Article).
- Mangin, J., 2002. A framework based on spin glass models for the inference of anatomical connectivity from diffusion-weighted mr data — a technical review. *NMR Biomed.* 15 (7-8), 481–492 (URL <http://dx.doi.org/10.1002/nbm.780>).
- Mori, S., Crain, B.J., Chacko, V.P., van Zijl, P.C., 1999. Three-dimensional tracking of axonal projections in the brain by magnetic resonance imaging. *Ann. Neurol.* 45 (2), 265–269 (99142739 0364-5134 Journal Article).
- Moseley, M.E., Cohen, Y., Kucharczyk, J., Mintorovitch, J., Asgari, H.S., Wendland, M.F., Tsuruda, J., Norman, D., 1990. Diffusion-weighted mr imaging of anisotropic water diffusion in cat central nervous system. *Radiology* 176 (2), 439–445 (0033-8419 Journal Article).
- Neal, R.M., 1993. Probabilistic Inference Using Markov Chain Monte Carlo Methods.
- Parker, G.J.M., Haroon, H.A., Wheeler-Kingshott, C.A.M., 2003. A framework for a streamline-based probabilistic index of connectivity (pico) using a structural interpretation of MRI diffusion measurements. *J. Magn. Reson. Imaging* 18 (2), 242–254 (english 1053-1807).
- Poupon, C., Rieul, B., Kezele, I., Perrin, M., Poupon, F., Mangin, J., 2008. New diffusion phantoms dedicated to the study and validation of high-angular-resolution diffusion imaging (hardi) models. *Magn. Reson. Med.* 60 (6), 1276–1283 (Dec).
- Reisert, M., Mader, I., Kiselev, V., 2009. Global reconstruction of neuronal fibres. *Proceedings of MICCAI, Diffusion Modelling Workshop*.
- Saur, D., Kreher, B.W., Schnell, S., Kummerer, D., Kellmeyer, P., Vry, M.-S., Umarova, R., Musso, M., Glauche, V., Abel, S., Huber, W., Rijntjes, M., Hennig, J., Weiller, C., 2008. Ventral and dorsal pathways for language. *Proc. Natl. Acad. Sci. USA* 105 (46), 18035–18040.
- Tournier, J., Calamante, F., Gadian, D., Connelly, A., 2007. Robust determination of the fibre orientation distribution in diffusion MRI: non-negativity constrained super-resolved spherical deconvolution. *Neuroimage* 35 (4), 1459–1472 (URL <http://www.sciencedirect.com/science/article/B6WNP-4N3P-065-5/2/43afd9f1d21cafe00341f12cae7bf55b>).
- van Lieshout, M.N.M., 2000. Markov Point Processes and Their Applications. Imperial College Press, London.